

# Monolithic III-V Nanowire Solar Cells on Graphene via Direct van der Waals Epitaxy

Parsian K. Mohseni, Ashkan Behnam, Joshua D. Wood, Xiang Zhao, Ki Jun Yu, Ning C. Wang, Angus Rockett, John A. Rogers, Joseph W. Lyding, Eric Pop, and Xiuling Li\*

Over the past two decades, research in the field of semiconductor nanowires (NWs) has helped to reshape our understanding of atomic-scale crystal assembly<sup>[1–3]</sup> and uncover novel physical phenomena at the nanometer scale.<sup>[4–6]</sup> Compound semiconductor NWs have also been established as central components in next-generation electronic<sup>[7–9]</sup> and photonic<sup>[10–12]</sup> devices. In particular, extensive investigations are currently being pursued to more effectively exploit the advantages offered by NWs composed of III-V compounds for photovoltaic (PV) energy conversion applications.<sup>[13,14]</sup>

For photovoltaics, NWs offer three main advantages, as compared to conventional bulk-crystalline or thin-film solar cells. They permit enhanced absorption of solar radiation by extending the absorption cross-section beyond the geometric footprint of a single NW,<sup>[15]</sup> by causing otherwise reflected broadband incident light to be absorbed in a NW array configuration through multiple scattering interactions,<sup>[16–18]</sup> and by generating a graded effective refractive index from air to the light-absorbing matrix for more efficient light coupling.<sup>[19]</sup> NWs also permit three-dimensional variations in doping<sup>[20–22]</sup> and heterostructure<sup>[23–25]</sup> profiles through coaxial geometries. This is particularly beneficial for efficient collection of photogenerated carriers when core and shell segments are engineered to be thinner than minority carrier diffusion lengths.<sup>[26]</sup> Finally, NWs are more conducive to heterogeneous integration solutions, owing to the nature of the NW geometry to accommodate heteroepitaxially-induced strain by relaxation along the NW free surface.<sup>[9,23]</sup> This advantage effectively increases the critical thickness of lattice-mismatched NW crystals in comparison to epi-layers having a purely planar geometry.<sup>[27–29]</sup> Therefore, NW array-based architectures are attractive for multi-junction PVs, insofar as high-efficiency devices relying on the monolithic integration of III-V materials with Si technology have been envisioned.<sup>[30–32]</sup>

An additional benefit of the use of NW arrays for PVs is the inherent cost-saving potential associated with the reduced volume of the energy conversion medium, leveraged by the ability to grow high quality III-V crystals on foreign substrates. The use of foreign (non-III-V compound semiconductor) substrates was previously shown to enhance device functionality through added mechanical flexibility, as well as circumvent the need for ex-situ electrical contacting schemes.<sup>[33]</sup> Since the principal goal of third-generation PVs is not only the continual increase of power conversion efficiencies, but also the reduction of solar cell development costs, such novel hybrid materials can provide a practical solution. Motivated by this principle, here we present a novel solar cell architecture utilizing a dense array of vertically oriented and axially heterostructured NWs with radial p–n junctions and in situ inorganic passivation layers, grown monolithically on graphene through direct van der Waals epitaxy by metal-organic chemical vapor deposition (MOCVD). Using this hybrid material system, we demonstrate power conversion efficiencies as high as 2.51%, which is greater than what has been previously achieved using the same material systems even on bulk crystalline substrates with similar NW-based designs.<sup>[14]</sup> We highlight the main benefits of this III-V photovoltaic solar cell design as one that is low-cost, substrate-free, and with a built-in back side contact, while being conducive to integration within other flexible device platforms.

In a recent study, we established the preferential phase-segregation of InGaAs during van der Waals epitaxial self-assembly of NWs on graphene.<sup>[34]</sup> Herein, we demonstrate that single-phase InGaAs NWs can be grown on graphene through the incorporation of an intermediate InAs “pedestal” segment. **Figure 1a** shows a tilted-view scanning electron microscopy (SEM) image obtained from an as-grown sample containing axially heterostructured InGaAs/InAs NWs on a monolayer sheet of graphene. Much like previous growths of the same kind,<sup>[34–36]</sup> we note that all NWs are vertically oriented and exhibit no tapering along their axial profiles. Additionally, no seed particles or foreign material collection agents are found at the tips of the NWs, in contrast to conventional NW growth relying on the metal-seeded vapor-liquid-solid (VLS) mechanism. Instead, the current growth method relies on pseudo-Volmer-Weber direct epitaxial assembly of discrete InAs islands on graphene, with (111) oriented top surfaces. Following island formation, anisotropic crystal growth likely proceeds at elevated rates along the energetically favorable <111> direction, similar to the case of selective area epitaxy (SAE) of semiconductor NWs. This forms hexagonally faceted NWs extending

Dr. P. K. Mohseni, Dr. A. Behnam, Dr. J. D. Wood,  
X. Zhao, N. C. Wang, Prof. J. W. Lyding,  
Prof. E. Pop, Prof. X. Li  
Department of Electrical and Computer Engineering  
University of Illinois at Urbana-Champaign  
Urbana, Illinois 61801, USA  
E-mail: xiuling@illinois.edu

K. J. Yu, Prof. A. Rockett, Prof. J. A. Rogers  
Department of Materials Science and Engineering  
University of Illinois at Urbana-Champaign  
Urbana, Illinois 61801, USA

DOI: 10.1002/adma.201305909



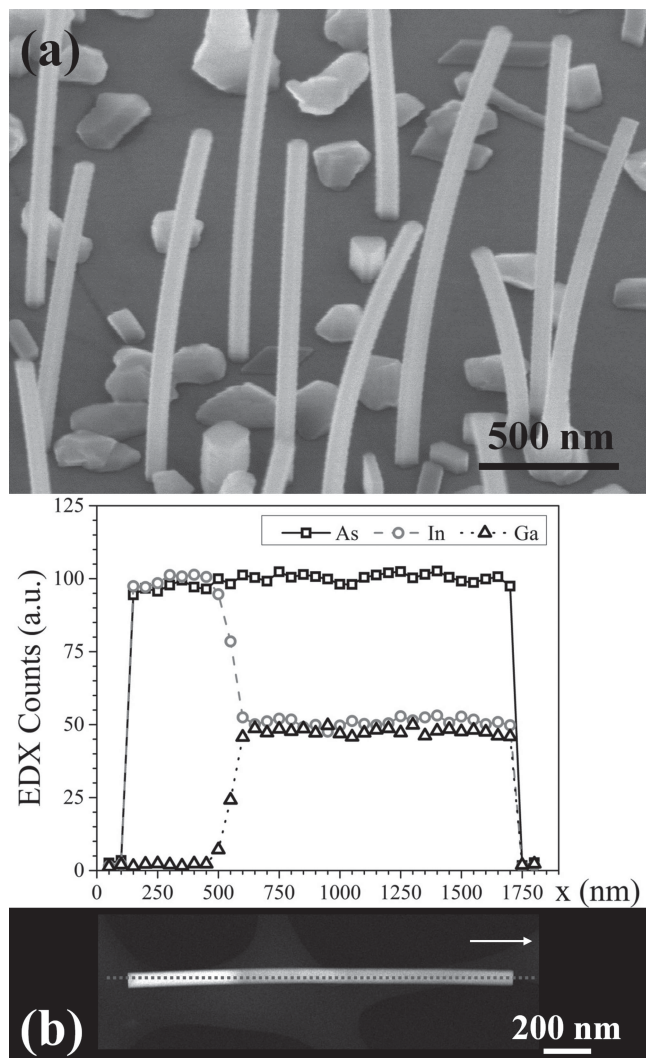


**Figure 1.** a) Tilted-view SEM images of as-grown, axially heterostructured InGaAs/InAs NWs on graphene substrates. b) HAADF-STEM image of a single InGaAs/InAs NW obtained from the same samples as shown in (a) and corresponding EDXS linescan obtained along the location of the dashed blue line. Elemental counts of As, In, and Ga are represented as black square, gray circle, and black triangle data points and curves, respectively. In the HAADF image, the region of bright (dark) contrast corresponds to a single compositional phase InAs (InGaAs) segment. The white arrow indicates the NW growth direction.

in length along the thermodynamically preferred direction and having  $\{-110\}$  sidewall planes. It should be noted that unlike VLS-type growth, where crystal phase purity may be achieved by appropriate tuning of crystal growth conditions, the direct epitaxy approach results in NWs with a polytypic crystal structure, similar to NWs grown through SAE.<sup>[9,34]</sup> At this point, no efforts have been directed by us or reported in the literature to control the polytypic phase change in direct epitaxy.

Structural and compositional investigations, by scanning transmission electron microscopy (STEM) analysis, reveal the axially heterostructured NW architecture. As can be seen in the high-angle annular dark-field (HAADF)-STEM image shown in Figure 1b, an extended region of dark contrast, corresponding

to a single-compositional phase of InGaAs, follows the region of bright contrast at the base of the NW, corresponding to the location of a binary InAs segment. Energy dispersive X-ray spectroscopy (EDXS) line-scan analysis, shown above the HAADF image in Figure 1b, confirms the composition of the InAs base and  $\text{In}_x\text{Ga}_{1-x}\text{As}$  body segments (in this case  $x = 0.55 \pm 0.02$ ). Interestingly, no morphological or crystal structure variances are observed upon the onset of InGaAs growth. Furthermore, no evidence for the formation of defects (dislocations, or otherwise) was observed near the heterointerface. This suggests that Ga incorporation proceeds according to a layer-by-layer growth regime over the previously assembled InAs base segment and that tensile strain can be accommodated by InGaAs segment without elastic relaxation.

Based on such axial heterostructure NW geometries, we carry out a solar cell performance optimization study by fabricating three sets of NW-based devices, each having distinct device architectures. The three device structures are schematically represented in Figure 2a–c. The first set of devices, henceforth termed group A devices, rely on NWs having an n-type InAs base segment followed by sequentially grown n-type (Si doping) and p-type (Zn doping)  $\text{In}_x\text{Ga}_{1-x}\text{As}$  ( $x \approx 0.25$ ) sections, as determined through previous composition optimization experiments. Therefore, group A solar cells contain axially segmented InGaAs/InAs NWs, which include a p–n junction within the InGaAs segment. In contrast, the second set of solar cells, termed group B devices, are fabricated using NWs that contain a radial p–n junction within their InGaAs segments, which are grown through a two-step MOCVD process. Finally, the third set of devices considered in this study, those referred to as group C devices, are fabricated through an identical process as group B, but contain an additional in situ grown p-type GaAs shell segment for surface passivation. Figure 2d shows a general schematic of the device structure, indicating the electrical contacting scheme. Specific details regarding growth of graphene films and NW arrays, their structural and geometric characteristics, as well as device fabrication are outlined in the Supporting Information (SI).

As depicted in Figures 2b,c, the base of the NWs are electrically isolated through the deposition of an  $\text{Al}_2\text{O}_3$  layer, such that short-circuit pathways along the Zn-doped shell to the graphene contact are effectively avoided. In this manner, the p-type InGaAs shell segments in the group B and C devices are engineered to encapsulate the n-type InGaAs core segment only. Specific details regarding this fabrication method, along with SEM images showing the various stages of the processing scheme, are shown in the SI (Figure S1).

The fabricated solar cells, composed of NW arrays on multi-layered graphene ( $n = 4$ ), were characterized through current-voltage ( $I$ – $V$ ) measurements obtained under dark and AM1.5G solar simulator illumination conditions. Figure 3a shows a comparison of the illuminated  $I$ – $V$  characteristics of the group A, B, and C devices as dotted, dashed, and solid curves, respectively, while the critical solar cell figures of merit based on these measurements are summarized in Table 1. We observe an increase in open-circuit voltage ( $V_{\text{OC}}$ ) from 0.18 V to 0.20 V with the transition from an axial (group A) to a radial (group B) junction profile. A more dramatic enhancement is noted upon surface passivation of the group C devices, marked by a  $V_{\text{OC}}$  of

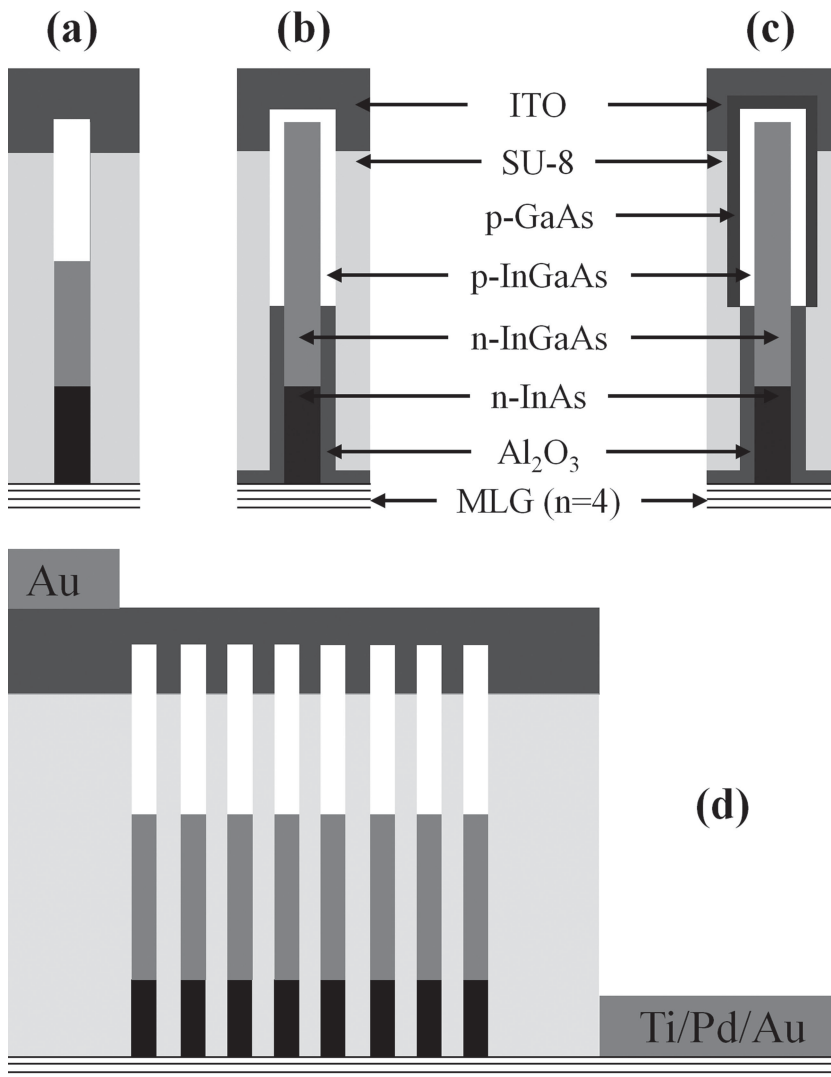


**Figure 2.** Schematic representation of the a) group A, b) group B, and c) group C NW-based device structures. d) Representation of the metallic contacting scheme as defined in the Experimental Details section of the Supporting Information. All substrates are depicted as multi-layer graphene (MLG) sheets ( $n = 4$ ).

0.26 V. An improvement in short-circuit current density ( $J_{SC}$ ) from  $13.14 \text{ mA cm}^{-2}$  to  $16.20 \text{ mA cm}^{-2}$  was also observed by changing from axial to radial junction devices. For the group C devices, surface passivation further improved  $J_{SC}$  to an optimal measured value of  $17.16 \text{ mA cm}^{-2}$ . The combined effects of implementing a radial junction geometry and surface passivation also resulted in a substantial increase in the fill factor (FF) and power conversion efficiency (PCE) values of the group C devices to 55.32% and 2.51%, respectively. This equates to an increase by a factor of  $\approx 1.44$  in FF and a factor of  $\approx 2.76$  in PCE when comparing the performance of the groups A and C devices. Furthermore, while the groups A and B devices (both using non-passivated NWs) demonstrated comparably ideal factors of approximately  $n \approx 1.9$ , the surface passivation scheme employed in the case of group C solar cells resulted in a measured  $n \approx 1.54$  (refer to SI, Figures S2a). The implications of these

axial and radial extension of the existing NW structures was achieved. Through EDXS point analysis of single NW specimens, it was confirmed that the core InGaAs segments and re-grown InGaAs shells were of equivalent compositions, within the spatial and spectral resolution limit of the EDXS detector. Additional defects, besides already present stacking faults, were not introduced through this process. However, as shown in Figure S4 of the SI, the re-growth of GaAs passivation layers (group C samples) is associated with the formation of dislocations at the radial heterojunction, likely resulting from the elastic relaxation of the tensile strained shell segment, as previously observed by Popovitz-Biro and colleagues.<sup>[37]</sup>

Next, we consider the performance of the NW-based solar cells as a function of the device architecture. Implementation of a radial p-n junction, as opposed to an axial junction, leads to a modest increase in  $V_{OC}$ , but also gives a more considerable

performance specifications are discussed below. Further analysis regarding parasitic losses is presented in the SI (Figure S2b). It should be noted that neither diode-type  $I-V$  behavior under dark testing conditions nor photovoltaic effect under illuminated conditions was observed when purely n-type NWs with otherwise identical device structures were tested (SI, Figure S2c). Therefore, the observed solar cell performance is directly a consequence of the embedded p-n junction within the individual NWs, as opposed to Schottky barrier-associated diode behavior.<sup>[33]</sup>

In addition to illuminated  $I-V$  characterization, the external quantum efficiency (EQE) of the three solar cell groups was measured as a function of excitation wavelength. Figure 3b shows the comparison of EQE curves obtained from the three device structures, measured over a spectral range of 450–1100 nm. As indicated by the solid curve, the passivated NWs with radial junctions (group C devices) demonstrated an optimal EQE of approximately 71% at 970 nm, while peak EQE values of 46% and 49% were measured in the case of the group A (dotted curve) and group B (dashed curve) devices, respectively. It should be noted that a clear efficiency enhancement is observed in the case of the radial junction and surface-passivated device structure across the entire spectral range, most notably along the visible spectrum, which corresponds to the maximum irradiance range of the AM1.5G solar spectrum.

First, the effect of the NW re-growth process on crystal quality is considered. In the case of both group B and C devices, radial InGaAs segments of nominally equivalent composition are grown on existing InGaAs NWs over oxide-coated NW base segments. Structural analysis of re-grown InGaAs segments (SI, Figure S3) determined that both

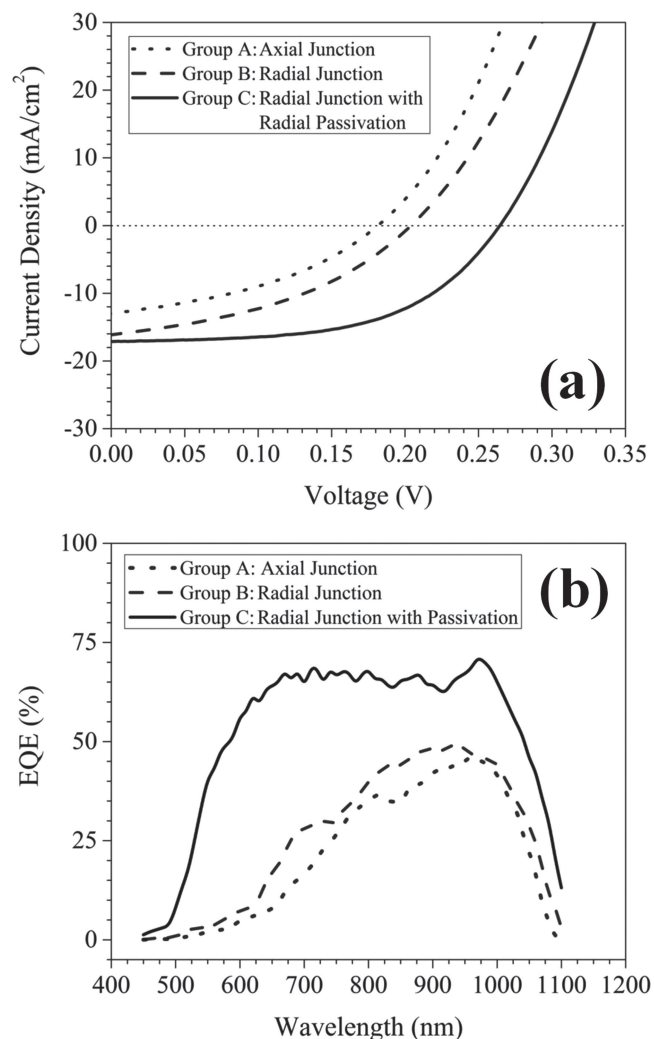


**Figure 3.** a) Illuminated (AM1.5G)  $I$ - $V$  characteristics and b) external quantum efficiency (EQE) spectra measured from the optimal performance group A (dotted curve), group B (dashed curve), and group C (solid curve) NW array-based solar cells.

increase in  $J_{SC}$ . This indicates that the radial junction profile allows carriers generated at various lengths along the NW to be effectively swept by the built-in electric field associated with the p-n junction. Conversely, in the case of the axial junction geometry, carriers generated further from the depletion region are more likely to undergo Shockley-Read-Hall (SRH) recombination. The effect of the junction geometry is also discerned from the EQE measurements (Figure 3b); insofar as a greater fraction of photogenerated carriers are collected at all excitation

wavelengths for the group B versus group A devices. Based on the measured FF values and the curvature of the illuminated  $I$ - $V$  curves shown in Figure 3a, we note that neither series nor shunt resistances are affected by the junction geometry significantly.

On the other hand, with the implementation of surface passivation for group C devices, the FF values are improved by approximately 15%, while a flat-line slope at the short-circuit current density point seen in the illuminated  $I$ - $V$  curve of the passivated devices indicates that shunt resistances have been increased. Both of these features imply that surface defects and routes toward SRH recombination have been effectively quenched with the introduction of passivating NW shell segments. Furthermore, as noted in Table 1, group C devices show a large (60 mV) enhancement in  $V_{OC}$ , despite only a  $\approx 1$  mA cm<sup>-2</sup> increase in  $J_{SC}$ . This was previously reported as a signature of effective carrier recombination suppression upon surface passivation.<sup>[38]</sup> Also notable is the ideality factor reduction from 1.91 to 1.54 with the implementation of surface passivation, which further demonstrates that the addition of outer GaAs shell segments allows for lower surface recombination rates. Finally, the most striking difference in the group C devices is the observed EQE enhancement toward the lower wavelength spectral range. Here, we note that although group A and B devices both show a gradual decrease in EQE below 800 nm, the group C devices show no signs of EQE reduction above  $\approx 600$  nm. It should be noted that this range corresponds to the maximum irradiance regime of the AM1.5G solar spectrum as well as the spectral range of minimum reflectance as measured from our arrays of NWs grown on graphene (refer to SI, Figure S5). As previously observed by Mariani et al. for the case of SAE-grown GaAs NW arrays with InGaP passivation layers,<sup>[39]</sup> such EQE trends likely arise from the collection of carriers generated near the NW surfaces from the absorption of high energy incident photons. As high energy photon absorption occurs at relatively lower penetration depths, the higher EQE values in this spectral range, while absent in the non-passivated devices, can be associated with the effective reduction of active surface recombination sites in group C devices.

Another important consideration is related to the role of interfacial defects arising from GaAs shell growth. We emphasize that the effect of suitable passivation schemes largely outweighs the effect of improved junction geometries. Furthermore, comparison of FF and PCE values of the group B and C devices leads us to conclude that the benefits of surface passivation outweigh the detriments of heteroepitaxially induced dislocations at the GaAs/InGaAs interface. Therefore, although the introduction of GaAs segments causes the formation of dislocations, the associated surface trap density reduction effects are more influential in terms of PCE enhancement.

**Table 1.** The main performance parameters and figures of merits obtained from the optimal NW-array on graphene solar cells presented in this study.

Device Group	Device Structure	$V_{oc}$ (V)	$J_{sc}$ (mA cm <sup>-2</sup> )	FF (%)	PCE (%)	$n$
A	Axial Junction, No Passivation	0.18	13.14	38.43	0.91	1.93
B	Radial Junction, No Passivation	0.20	16.20	40.24	1.32	1.91
C	Radial Junction, GaAs Passivation	0.26	17.16	55.32	2.51	1.54

Next, we consider conduction at the InAs/graphene interface. For all solar cells fabricated in this study, multi-layer graphene (MLG,  $n = 4$ ) films were employed for improved conduction<sup>[40]</sup> and higher density NW growth (SI, Figure S6). In addition to serving as a pedestal for the growth of single-phase InGaAs segments, the InAs base segments grown on graphene also act as low band-gap and low series resistance point contacts and electron collection layers. In our previous study, we noted that along with NW growth on pristine graphene, island nucleation and growth also occurs, preferentially isolated to point or line defects on graphene films.<sup>[34]</sup> As shown in the SI (Figure S7), such islands aid to passivate the inherent defects of the graphene film. As part of this study, we carried out InAs growths under modified MOCVD conditions to yield only island structures on graphene films. It was determined that island growth aided in the passivation of graphene defects, such that a nearly two-fold increase in conductivity was observed in comparison to graphene control samples not subjected to InAs island growth. Similar to the study performed by Lee et al., where metallic nanowires on graphene films gave a significant reduction in graphene sheet resistance,<sup>[41]</sup> the preferential growth of InAs islands along graphene defects likely allows for mobile carriers, otherwise being scattered at the defect sites, to effectively bypass the scattering centers through conduction along the InAs islands. Therefore, both island formation and NW base InAs segment incorporations are expected reduce the series resistance in such semiconductor on graphene device architectures.

Finally, we compare the optimal device structure presented in the current work with several comparable PV designs published to date relying on arrays of III-V NWs on foreign substrates. Previously, our research group showed two distinct solar cells designs employing seed-free InGaAs<sup>[42]</sup> and InAsP<sup>[43]</sup> NWs grown directly on Si substrates. In both these approaches, n-type NWs were grown on p-type substrates, such that the active junction was coincident with the heterointerface between the III-V NWs and the Si substrate. Non-passivated InGaAs on Si devices showed an optimal PCE of 2.4%, while passivated InAsP on Si devices were capable of realizing 3.6% PCE under identical AM1.5G illuminated testing conditions as in the current study. Although these results are comparable to the performance of the current set of group C devices (~2.5% PCE), those previous devices were capable of absorbing incident solar illumination in both the NW arrays and the bulk crystalline substrates. In contrast, group C devices rely on graphene growth surfaces that provide negligible influence on the generation of carriers and thereby lower the optical substrate benefits. Alternative designs employing InAs (PCE = 1% at room temperature),<sup>[44]</sup> InN (PCE = 0.68%),<sup>[45]</sup> and InP-hybrid (PCE = 0.02%)<sup>[46]</sup> NW arrays on Si substrates have also been demonstrated. The key advantages of our device structure are as follows: the active junction is embedded directly within every NW comprising the energy harvesting array; the InAs pedestal segments at the base of the NWs allow for efficient collection of photogenerated electrons; and, finally, the passivation layers effectively prohibit the recombination of electron-hole pairs generated by photons absorbed from the higher energy spectral range. We also highlight the use of graphene as the growth surface, which not only introduces significant cost

benefits when compared to the use of III-V or Si substrates, but also provides the potential for fabrication of flexible devices. Although III-V NWs on carbon-based substrates for PV applications have been previously reported,<sup>[33]</sup> the current approach employing graphene ensures vertical orientation of NWs and an abrupt epitaxial growth front, both being necessary criteria for the formation of suitable electrical contacts to NW arrays. Higher conversion efficiency values are anticipated if optimal bandgap materials, such as InP, are used, and with further optimization of the device design for the mitigation of the following loss mechanisms: 1) non-ideal surface passivation material, i.e., InP or AlInP instead of GaAs; 2) series resistances arising from NW/ITO interface and graphene contacts; 3) non-uniformity of NW height distribution for electrical contact to all NWs in the array; and 4) valance band energy barrier at GaAs/InGaAs interface for hole collection. Upon reduction of these losses through future design optimization, we anticipate that such NW-array-on-graphene architectures can be employed as supplementary components in stacked, hierarchical devices as energy converters, light emitters, or sensors.

In summary, we have presented a novel solar cells design employing InGaAs/InAs heterostructured NW arrays grown directly by van der Waals epitaxy on graphene films. A device performance optimization study was carried out through which the role of axial versus radial NW p-n junctions and the influence of in situ surface passivation were distinguished. We have concluded that radial junction geometries show moderate PCE enhancement as compared to axial junction geometries. Furthermore, we have determined that the addition of surface passivation shell segments greatly outweigh the benefits gained from implementation of a radial NW junction design as well as the detrimental effects of misfit dislocations suffered from the formation of lattice mismatched passivating shell segments. The solar cell structures employing surface passivation shell layers and co-axial p-n junction In<sub>0.25</sub>Ga<sub>0.75</sub>As NW geometries on graphene achieved a PCE of 2.51%, which is a new performance record for III-V NWs with embedded junctions grown on graphene. Although In<sub>0.25</sub>Ga<sub>0.75</sub>As is not the optimum band-gap material for high efficiency solar cells, the direct epitaxy on graphene platform established here has significant implications for a wide variety of III-V compound semiconductor NW-based devices on graphene, such as light emitters and multi-junction tandem solar cells, all of which can be released for flexible applications. Additional geometrical considerations such as NW length, diameter, spacing, and array configuration are expected to further improve the broadband absorption and photocurrent generation of the current devices.

## Supporting Information

Supporting Information is available from the Wiley Online Library or from the author.

## Acknowledgements

P.K.M. kindly thanks Dr. Julio A. Soares for assistance with EQE measurements. P.K.M., X.Z., K.J.Y., J.A.R., and X.L. were supported in part by the U.S. Department of Energy, Office of Basic Energy Sciences, Division of Materials Sciences and Engineering under Award

#DE-FG02-07ER46471, through the Frederick Seitz Materials Research Laboratory at the University of Illinois at Urbana-Champaign. A.B., J.D.W., E.P., and J.W.L. were supported in part by the Office of Naval Research grants N00014-10-1-0853. J.D.W. gratefully acknowledges financial support from the Beckman Foundation and the National Defense Science and Engineering Graduate (NDSEG) fellowship.

Received: December 1, 2013

Revised: January 16, 2014

Published online: March 20, 2014

- [1] M. T. Borgström, G. Immink, B. Ketelaars, R. Algra, E. P. A. M. Bakkers, *Nat. Nanotechnol.* **2007**, *2*, 541.
- [2] H. Johansson, L. S. Karlsson, C. P. T. Svensson, T. Martensson, B. A. Wacaser, K. Deppert, L. Samuelson, W. Seifert, *Nat. Mater.* **2006**, *5*, 574.
- [3] K. A. Dick, P. Caroff, J. Bolinsson, M. E. Messing, J. Johansson, K. Deppert, L. R. Wallenberg, L. Samuelson, *Semincond. Sci. Technol.* **2010**, *25*, 024009.
- [4] H. Wang, L. A. Zepeda-Ruiz, G. H. Gilmer, M. Upmanyu, *Nature Commun.* **2013**, *4*, 1956.
- [5] A. D. K. Finck, D. J. Van Harlingen, P. K. Mohseni, K. Jung, X. Li, *Phys. Rev. Lett.* **2013**, *110*, 126406.
- [6] V. Mourik, K. Zuo, S. M. Frolov, S. R. Plissard, E. P. A. M. Bakkers, L. P. Kouwenhoven, *Science* **2012**, *336*, 1003.
- [7] X. Miao, C. Zhang, X. Li, *Nano Lett.* **2013**, *13*, 2548.
- [8] K. Storm, G. Nylund, L. Samuelson, A. P. Micolich, *Nano Lett.* **2012**, *12*, 1.
- [9] K. Tomioka, M. Yoshimura, T. Fukui, *Nature* **2012**, *488*, 189.
- [10] M. P. van Kouwen, M. H. M. van Weert, M. E. Reimer, N. Akopian, U. Perinetti, R. E. Algra, E. P. A. M. Bakkers, L. P. Kouwenhoven, V. Zwiller, *Appl. Phys. Lett.* **2010**, *97*, 113108.
- [11] M. E. Reimer, G. Bulgarini, N. Akopian, M. Hocevar, M. B. Bavinck, M. A. Verheijen, E. P. A. M. Bakkers, L. P. Kouwenhoven, V. Zwiller, *Nature Commun.* **2012**, *3*, 737.
- [12] B. Hua, J. Motohisa, Y. Kobayashi, S. Hara, T. Fukui, *Nano Lett.* **2009**, *9*, 112.
- [13] K. Sun, A. Kargar, N. Park, K. N. Madsen, P. W. Naughton, T. Bright, Y. Jing, D. Wang, *IEEE J. Sel. Top. Quantum Electron.* **2011**, *17*, 1033.
- [14] R. R. LaPierre, A. C. E. Chia, S. J. Gibson, C. M. Haapamaki, J. Boulanger, R. Yee, P. Kuyanov, J. Zhang, N. Tajik, K. M. A. Rahman, *Phys. Status Solidi RRL* **2013**, *7*, 815.
- [15] P. Krogstrup, H. I. Jørgensen, M. Heiss, O. Demichel, J. V. Holm, M. Aagesen, J. Nygård, A. Fontcuberta i Morral, *Nat. Photonics* **2013**, *7*, 306.
- [16] O. L. Muskens, J. G. Rivas, R. E. Algra, E. P. A. M. Bakkers, A. Lagendijk, *Nano Lett.* **2008**, *8*, 2638.
- [17] P. M. Wu, N. Anttu, H. Q. Xu, L. Samuelson, M.-E. Pistol, *Nano Lett.* **2012**, *12*, 1990.
- [18] N. Huang, C. Lin, M. L. Povinelli, *J. Opt.* **2012**, *14*, 024004.
- [19] J.-Y. Jung, Z. Guo, S.-W. Jee, H.-D. Um, K.-T. Park, J.-H. Lee, *Opt. Express* **2010**, *18*, A286.
- [20] J. A. Czaban, D. A. Thompson, R. R. LaPierre, *Nano Lett.* **2009**, *9*, 148.
- [21] P. K. Mohseni, G. Lawson, C. Couteau, G. Weihs, A. Adronov, R. R. LaPierre, *Nano Lett.* **2008**, *8*, 4075.
- [22] B. Tian, X. Zheng, T. J. Kempa, Y. Fang, N. Yu, G. Yu, J. Huang, C. M. Lieber, *Nature* **2007**, *449*, 885.
- [23] P. K. Mohseni, C. Maunders, G. A. Botton, R. R. LaPierre, *Nanotechnology* **2007**, *18*, 445304.
- [24] P. K. Mohseni, A. D. Rodrigues, J. C. Galzerani, Y. A. Pusep, R. R. LaPierre, *J. Appl. Phys.* **2009**, *106*, 124306.
- [25] P. K. Mohseni, R. R. LaPierre, *Nanotechnology* **2009**, *20*, 025610.
- [26] B. M. Kayes, H. A. Atwater, N. S. Lewis, *J. Appl. Phys.* **2005**, *97*, 114302.
- [27] G. E. Cirlin, V. G. Dubrovskii, I. P. Soshnikov, N. V. Sibirev, Yu. B. Samsonenko, A. D. Bouravleuv, J. C. Harmond, F. Glas, *Phys. Status Solidi RRL* **2009**, *3*, 112.
- [28] E. Ertekin, P. A. Greaney, D. C. Chrzan, *J. Appl. Phys.* **2005**, *91*, 114325.
- [29] F. Glas, *Phys. Rev. B* **2006**, *74*, 121302.
- [30] R. R. LaPierre, *J. Appl. Phys.* **2011**, *110*, 014310.
- [31] Y. Hu, M. Li, J. J. He, R. R. LaPierre, *Nanotechnology* **2013**, *24*, 065402.
- [32] S. Bu, X. Li, L. Wen, X. Zeng, Y. Zhao, W. Wang, Y. Wang, *Appl. Phys. Lett.* **2013**, *102*, 031106.
- [33] P. K. Mohseni, G. Lawson, A. Adronov, R. R. LaPierre, *IEEE J. Sel. Top. Quantum Electron.* **2011**, *17*, 1070.
- [34] P. K. Mohseni, A. Behnam, J. D. Wood, C. D. English, J. W. Lyding, E. Pop, X. Li, *Nano Lett.* **2013**, *13*, 1153.
- [35] Y. J. Hong, W. H. Lee, Y. Wu, R. S. Ruoff, T. Fukui, *Nano Lett.* **2012**, *12*, 1431.
- [36] A. M. Munshi, D. L. Dheeraj, V. T. Fauske, D.-C. Kim, A. T. J. van Helvoort, B.-O. Fimland, H. Weman, *Nano Lett.* **2012**, *12*, 4570.
- [37] R. Popvitz-Biro, A. Kretinin, P. Von Huth, H. Shtrikman, *Cryst. Growth. Des.* **2011**, *11*, 3858.
- [38] J. V. Holm, H. I. Jørgensen, P. Krogstrup, J. Nygård, H. Liu, M. Aagesen, *Nature Commun.* **2013**, *4*, 1498.
- [39] G. Mariani, A. C. Scofield, C.-H. Hung, D. L. Huffaker, *Nature Commun.* **2013**, *4*, 1497.
- [40] J. M. Lee, J. W. Choung, J. Yi, D. H. Lee, M. Samal, D. K. Yi, C.-H. Lee, G.-C. Yi, U. Paik, J. A. Rogers, W. I. Park, *Nano Lett.* **2010**, *10*, 2783.
- [41] M.-S. Lee, K. Lee, S.-Y. Kim, H. Lee, J. Park, K. H. Choi, H.-K. Kim, D.-G. Kim, D. Y. Lee, S. W. Nam, J.-U. Park, *Nano Lett.* **2013**, *13*, 2814.
- [42] J. C. Shin, H. K. Kim, K. J. Yu, H. Hu, L. Yin, C. Z. Ning, J. A. Rogers, J.-M. Zuo, X. Li, *Nano Lett.* **2011**, *11*, 4831.
- [43] J. C. Shin, A. Lee, P. K. Mohseni, D. Y. Kim, L. Yu, J. H. Kim, H. J. Kim, W. J. Choi, D. Wasserman, K. J. Choi, X. Li, *ACS Nano* **2013**, *7*, 5463.
- [44] W. Wei, X.-Y. Bao, C. Soci, Y. Ding, Z.-L. Wang, D. Wang, *Nano Lett.* **2009**, *9*, 2926.
- [45] H. Pham, T. Nguyen, Y.-L. Chang, I. Shih, Z. Mi, *IEEE J. Sel. Top. Quantum Electron.* **2011**, *17*, 1062.
- [46] C. J. Novotny, E. T. Yu, P. K. L. Yu, *Nano Lett.* **2011**, *8*, 775.